[1] Pengmou Ma
[2] Sibo Liu
[3,*] Aijun Wang
[4] Xiaomei He

Precision Optimization Analysis of Online Measurement System for Laser Melting Pool Morphology in Additive Manufacturing Process

Journal of Electrical Systems

Abstract: **-** Selective Laser Melting (SLM), as the most precise and highest quality processing technology in additive manufacturing, is widely used in fields such as aerospace. Online measurement of the laser melting pool, the basic unit of the SLM process, reflects the precision and process stability of SLM. The accuracy of the online measurement system for laser melting pool morphology, which is based on the principle of visual measurement, is crucial for accurate evaluation of the laser melting pool morphology. This paper firstly conducts research on visual calibration technology for the online measurement system of laser melting pool morphology, achieving precise positioning of the visual system and effectively calculating target-related feature information, which is then converted into corresponding digital information for further processing and analysis. Secondly, the paper completes the system error analysis and parameter optimization design, effectively improving the accuracy of the visual measurement system. Finally, the optimized online measurement system is verified for accuracy and evaluated for precision, proving the feasibility and effectiveness of the methods presented in this paper.

Keywords: Selective Laser Melting (SLM); Online Measurement; Precision Analysis; Parameter Optimization

I. INTRODUCTION

Selective Laser Melting (SLM) technology, known for its high precision and capability to form complex precision structures, is widely used in fields such as aerospace, automotive manufacturing, mold making, energy and power, medical and health, etc [1]. SLM technology has gradually developed from the processing of high-precision small parts to penetrating various cutting-edge manufacturing fields [2]. SLM forming technology can be combined with subtractive manufacturing to achieve higher precision in parts processing [3]. The SLM equipment, integrating the strengths of all additive manufacturing devices, has become a pillar in the field of metal additive manufacturing. In the process of Selective Laser Melting, process parameters (morphological features of the melting pool, temperature field changes, splashing of the melting pool, plasma plume, etc.) are strongly correlated with the processing parameters of the SLM equipment (laser speed, laser power, laser spot diameter, layer thickness, scanning path, etc.). The stability of these processing parameters determines the precision and quality of the additively manufactured parts. Measuring and detecting the process parameters of additive manufacturing [4][5][6] is significant for dynamic monitoring of the SLM process parameters and quality control of the processed parts.

In recent years, the continuous advancement of machine vision technology has led to the widespread adoption of high-speed cameras for online monitoring of the SLM process. This technology enables the direct capture of morphological data pertaining to the melting pool throughout the processing stage [7][8]. Such information is instrumental in deducing key processing parameters and equipment status, thereby guiding the refinement of SLM equipment settings and enhancing the precision of final parts. This positively impacts the innovative development of intelligent additive manufacturing technology [9].

The online measurement system described in this paper adopts an off-axis structure built inside the (SLM) equipment. The SLM equipment operates under an inert gas protection environment to ensure that the oxygen content is below 0.1% for normal printing. The inclusion of the measurement system should not affect the internal processing environment and airflow. The overall schematic is shown in Figure 1. The system consists of a high-speed CMOS industrial camera, online measurement system mounting bracket, high-temperature camera insulation and sealing protection, FPGA high-speed processing chip, image acquisition card, high-speed image processing, and parameter evaluation software[10]. The parameters of the measurement system are shown in Table 1. The precision of the online measurement system, which relies on the principle of visual measurement to assess the laser

[1] Changcheng Institute of Metrology & Measurement, Aviation Industry Corporation of China, Beijing, China
[2] Changcheng Institute of Metrology & Measurement, Aviation Industry Corporation of China, Beijing, China
[3] Changcheng Institute of Metrology & Measurement, Aviation Industry Corporation of China, Beijing, China
[4] Changcheng Institute of Metrology & Measurement, Aviation Industry Corporation of China, Beijing, China
*Corresponding author:Aijun Wang

melting pool morphology during the additive manufacturing process, is of utmost importance for accurate evaluation of the laser melting pool morphology.

(a) Physical picture (b) Simulation diagram

Figure 1: Online Measurement System for Melting Pool Morphology in SLM Process

Table 1: Measurement System Indicators and Parameters

Parameter	Index
Resolution	2,336*1728 px
Pixel Size	7*7μm
Frame Rate	500fps
Field of View	65.408mm*48.364mm
Object Distance	300mm
Focal Length	50mm

During the shooting process, distortions and errors may arise due to factors such as the camera itself and external environmental conditions. Therefore, it is crucial to calibrate the camera to identify and compensate for these errors. Camera calibration serves as a fundamental step in machine vision, particularly in visual measurement. The accuracy of the calibration directly impacts the system's measurement precision. B. Hallet was the first to suggest the utilization of the least squares method for camera calibration, which involves establishing a pinhole imaging model for the camera. The renowned Tsai calibration method, a two-step approach, focuses on determining the camera's internal and external parameters based on this established model. As machine vision technology gained popularity, Zhengyou Zhang introduced the Zhang-style calibration method in 1988, which relies on a chessboard grid as a reference. In conclusion, various calibration methods possess distinct advantages and disadvantages, necessitating a selection that aligns with the specific measurement environment and requirements.

The methods for camera calibration, as shown in Table 2. Engineering technicians can choose the appropriate calibration method based on actual measurement and project needs. Considering the high measurement accuracy required by the measurement system described in this paper and taking into account the actual engineering applications, the Zhang-style calibration method was ultimately adopted.

Table 2: Measurement System Indicators and Parameters

Calibration Method Classification	Advantages	Disadvantages
Traditional Camera Calibration	Can be used with any camera model, high calibration accuracy	Complex calibration process, requires high-precision known structure information. In many practical applications, calibration blocks cannot be used.
Active Vision Camera Calibration	Usually allows for linear solutions and has high robustness	Not suitable for scenarios where camera motion is unknown and uncontrollable
Camera Self-Calibration	Only requires establishing correspondences between images; flexible, wide potential application range	Non-linear calibration, lower robustness

II. MEASUREMENT SYSTEM VISUAL CALIBRATION TECHNOLOGY

A. Principle

The camera calibration's underlying mathematical facet pertains to the establishment of a transformation relationship between the world coordinate system and the pixel coordinate system. The theoretical foundation of

this calibration lies in the camera's pinhole imaging model, which is graphically represented in Figure 2. The process involves using a camera to capture the feature points of a known image and solving for the camera model parameters. The principle of perspective transformation serves as the basis for the pinhole imaging model. The coordinate systems illustrated are: the image coordinate system (0,u,v), which is the pixel coordinate system in the image; the imaging coordinate system (0,x,y), which is the physical coordinate system of the image; the world coordinate system (WCS) (Ow,xw,yw,zw) used to describe the camera position; and the camera coordinate system (CCS) (Oc,xc,yc,zc), centered at the camera's optic center with the optical axis as zc, and xc,yc parallel to the imaging coordinate axes x and y.

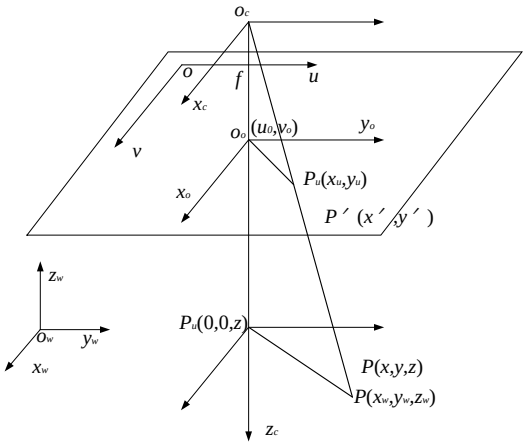

Figure 2: Camera Imaging Model Diagram

The transformation relationship between the Camera Coordinate System (CCS) and the World Coordinate System (WCS) is:

$$\begin{bmatrix} x_c \\ y_c \\ z_c \\ 1 \end{bmatrix} = \begin{bmatrix} R & T \end{bmatrix} \begin{bmatrix} x_w \\ y_w \\ z_w \\ 1 \end{bmatrix} \tag{1}$$

Where T=(tx,ty,tz), T represents the translation matrix;

R=R(α,β,γ) is the rotation matrix, determined by three rotation angles, α (around CCS's x-axis), β (around the y-axis), and γ (around the z-axis);

A, β, γ, tx, ty, tz are the six parameters of R,T, constituting the external parameters of the camera.

$$R(\alpha,\beta,\gamma) = \begin{pmatrix} 1 & 0 & 0 \\ 0 & \cos\alpha & -\sin\alpha \\ 0 & \sin\alpha & \cos\alpha \end{pmatrix} \begin{pmatrix} \cos\beta & 0 & \sin\beta \\ 0 & 1 & 0 \\ -\sin\beta & 0 & \cos\beta \end{pmatrix} \begin{pmatrix} \cos\gamma & -\sin\gamma & 0 \\ \sin\gamma & \cos\gamma & 0 \\ 0 & 0 & 1 \end{pmatrix} \tag{2}$$

From Equation (2), we obtain the three-dimensional points in the camera coordinate system, and from the collinear equations in visual measurement, the relationship between the camera coordinate system and the image coordinate system:

$$u = f\frac{x_c}{z_c} \tag{3}$$

$$v = f\frac{y_c}{z_c} \tag{4}$$

Where f is the camera focal length.

The above describes camera calibration using the pinhole imaging model in an ideal state. In actual visual measurement, internal errors in the camera are unavoidable. The difference between the actual image center point O(u0,v0) and the theoretical center point O1 (u01,v01) is (△u,△v):

$$\Delta u = u_{01} - u_0 \tag{5}$$

$$\Delta v = v_{01} - v_0 \tag{6}$$

In actual imaging, cameras exhibit certain distortions. Camera distortions are divided into radial and tangential distortions, with radial distortion being the primary concern, and tangential distortion often neglected in practical measurements. Radial distortion is represented as △r

$$\Delta r = k_0 r \quad + k_1 r^3 + k_2 r^5 + k_3 r^7 + k_4 r^9 + \ldots \tag{7}$$

where r is the distance from the image point to the principal point;

k0, k1, k2, ... are the distortion coefficients.

In the u and v directions, the projection of △r is:

$$\Delta x = -x\frac{\Delta r}{r} = -x(k_0 r \quad + k_1 r^2 + k_2 r^4 + \ldots) \tag{8}$$

$$\Delta y = -y\frac{\Delta r}{r} = -y(k_0 r \quad + k_1 r^2 + k_2 r^4 + \ldots) \tag{9}$$

B. Zhang's Calibration Method

Zhang's Calibration Method uses a chessboard grid pattern as the calibration image. Several template images are captured from different angles, and feature points in the images are detected. These feature points are used to calculate the internal and external parameters of the camera and to determine distortion parameters, ultimately optimizing and refining the results, as shown in Figure 3.

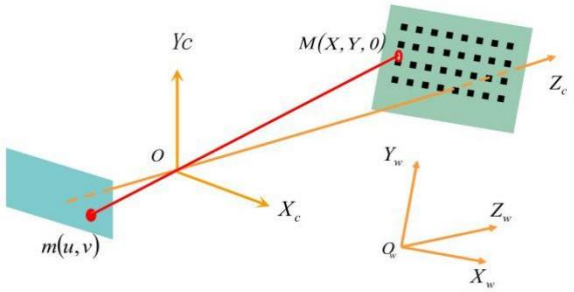

Figure 3: Diagram of Zhang's Calibration Method

The basic principle of Zhang's Calibration Method is:

$$s\begin{bmatrix} u \\ v \\ 1 \end{bmatrix} = K\begin{bmatrix} r_1 & r_2 & r_3 & t \end{bmatrix}\begin{bmatrix} X \\ Y \\ 0 \\ 1 \end{bmatrix} = K\begin{bmatrix} r_1 & r_2 & t \end{bmatrix}\begin{bmatrix} X \\ Y \\ 1 \end{bmatrix} \tag{10}$$

The homogeneous coordinates on the template plane are:

$$\widetilde{M} = \begin{bmatrix} X & Y & 1 \end{bmatrix}^T \tag{11}$$

The homogeneous coordinates of the corresponding points projected onto the image plane are:

$$\widetilde{m} = \begin{bmatrix} u & v & 1 \end{bmatrix}^T \tag{12}$$

Assuming the template plane is in the World Coordinate System (WCS) on the plane Z=0, where K is the camera's intrinsic matrix, [r1,r2,r3] and T are the rotation matrix and translation vector.

Let:

$$H = \begin{bmatrix} h_1 & h_2 & h_3 \end{bmatrix} = \lambda K\begin{bmatrix} r_1 & r_2 & t \end{bmatrix} \tag{13}$$

Then:

$$r_1 = \frac{1}{\lambda}K^{-1}h_1, \quad r_2 = \frac{1}{\lambda}K^{-1}h_2 \tag{14}$$

From the properties of the rotation matrix, we know:

$$r_1^T r_2 = 0 \quad \|r_1\| = \|r_2\| = 1 \tag{15}$$

Thus, each image provides two fundamental constraints for the intrinsic matrix. That is:

$$h_1^T K^T K^{-1} h_2 = 0 \tag{16}$$

$$h_1^T K^T K^{-1} h_1 = h_2^T K^T K^{-1} h_2 \tag{17}$$

As the camera has five unknown parameters, when the number of feature images captured is greater than or equal to 3, a unique K can be linearly solved.

In this paper, Zhang's Calibration Method is used to calibrate the measurement system: the calibration board used is the GQ-F63-3 type chessboard grid. Subsequently, the camera is calibrated using the Camera Calibrator in Matlab2021. The calibration process involves first selecting a chessboard grid image and obtaining the size of each square on the grid (in this paper, each square is 3.0mm in size), then detecting feature corner points on the chessboard grid calibration board image, as shown in Figure 4(b). Next, information from all corners of the chessboard grid calibration board is obtained, and finally, the calibration begins to obtain the camera's intrinsic parameter matrix. As shown in Figure 5:

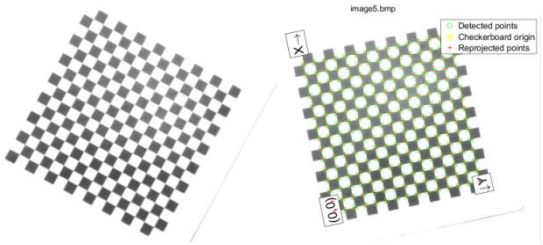

(a) Chessboard grid image captured by the camera (b) Extracted feature points of the chessboard grid

Figure 4: Chessboard Grid Calibration

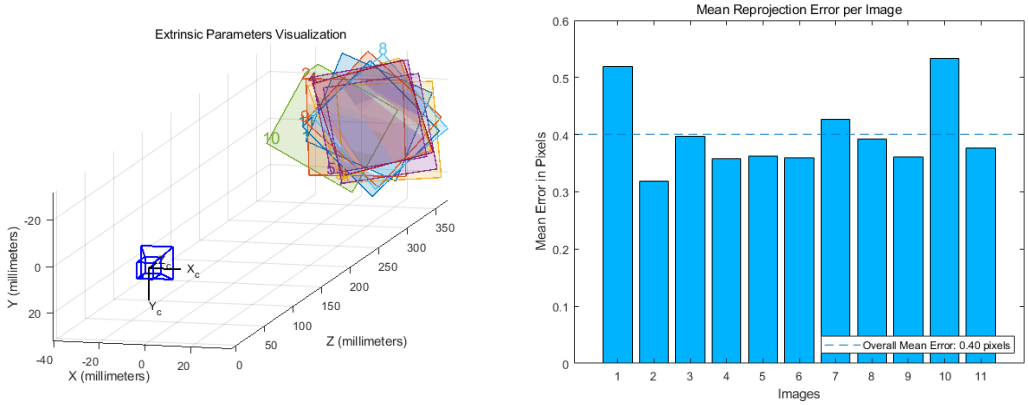

(a) Camera center position (b) Error

Figure 5: Camera Pose and Error

C. Calibration Result Analysis

This paper employed Zhang's Calibration Methodology to calibrate the measurement system, and subsequently validated the calibration outcomes through the utilization of a glass graticule ruler. The glass graticule ruler serves as a highly precise reference measuring device, widely utilized in the calibration of diverse measuring instruments. Within this research, an image processing algorithm was utilized to extract the scale values from the glass graticule ruler, enabling the computation and comparison of actual scale values against theoretical ones. Figure 6 illustrates the glass graticule ruler captured by the measurement system, with the finest scale resolution being 1.0 mm. By extracting adjacent scale values, specifically two adjacent scale values, and five adjacent scale values from diverse camera images and poses, the measurement outcomes are presented in Table 3.

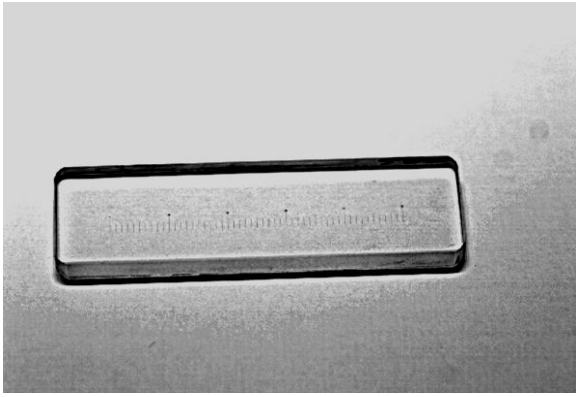

Figure 6: Glass Graticule Ruler

After camera calibration, the measurement error of the online measurement system remains between 0.01 and 0.05mm. The measurement accuracy is insufficient for the research of the online measurement system, so accuracy compensation and parameter optimization design are necessary to meet the high-precision measurement requirements.

Table 3: Measurement Results Obtained from Extracting Adjacent Scale Values (Unit: mm)

Measurement Number	1.0mm Scale Value Measurement Result	2.0mm Scale Value Measurement Result	5.0mm Scale Value Measurement Result
1	1.018	2.035	5.036
2	1.017	2.039	4.992
3	1.017	1.965	4.988
4	1.020	1.961	5.041
5	1.024	1.959	5.041
6	1.027	1.958	5.042
7	1.030	1.963	5.043
8	1.032	1.969	5.046
9	1.032	2.028	5.047
10	1.035	1.962	4.962
11	0.986	1.974	4.971
12	0.944	2.022	4.99
13	0.953	2.013	5.028
14	0.909	2.014	5.022
15	0.958	2.012	4.964
16	0.956	2.017	4.982
17	0.979	1.99	5.029
18	0.975	1.988	5.034
19	0.961	1.962	5.038
20	0.958	1.968	5.04

III. System Error Analysis and Parameter Optimization Design

The camera's internal and external parameter matrix has been obtained through Zhang's Calibration Method. However, when calibrating the online measurement system for the additive manufacturing process melting pool morphology with a high-precision glass graticule ruler, the measurement results do not meet the required accuracy. There are two methods for compensating the accuracy of the measurement system: global accuracy compensation for measurement results and optimization of the camera's internal and external parameters. Using global accuracy compensation for measurement results requires an additional step of calculation before outputting the final results, which is not conducive to the online measurement data processing. Therefore, this paper adopts the method of optimizing the camera's internal and external parameters for the accuracy compensation of the measurement system, iterating, and optimizing the parameters after calibration. In the iterative optimization design, the impact of different camera parameters on the measurement accuracy is fully considered, and a more accurate camera parameter matrix is obtained.

A. Theoretical Analysis of Camera Parameter Optimization

In practical visual measurement, The transformation between the world coordinate system and the image coordinate system is achieved through the utilization of the camera's internal and external parameter matrices. The camera calibration procedure involves the determination of these parameters, which inevitably contain errors and are not entirely precise. This implies a deviation between the actual observed values and the values predicted by the mathematical model. This deviation within the camera parameter mathematical model is referred to as a residual.

The optimization procedure strives to consistently refine the camera's internal and external parameters to minimize the target residual [13]. Specifically, in the context of camera calibration, the pixel residual serves as the target residual. By leveraging the camera's internal and external parameters along with the world coordinates of the feature points, the actual pixel coordinates are derived. The discrepancy between the pixel coordinates represented in the image and the actual coordinates constitutes the target residual.

The optimization function is:

$$E_m = \left\| \left[x - \bar{x}(K[R \quad t], M) \right]^2 + \left[y - \bar{y}((K[R \quad t], M)) \right]^2 \right\| \tag{18}$$

Where K[R t] represents the camera's internal and external parameters;

M is the coordinate value of a point in the world coordinate system, $M = (x_{wi}, \ y_{wi}, \ z_{wi},) \ \ i = 1,2,\ldots,M$

The optimization of K[R t] aims to minimize the residual Em:

$$\frac{dE_m}{d\left(K[R \quad t]\right)} = 0 \tag{19}$$

In the optimization design of this paper, the estimated values of the camera's internal and external parameters have already been obtained through Zhang's Calibration Method. Equations (18) and (19) are common methods for camera parameter optimization. Based on the above research, this paper uses points on the scale lines of the high-precision glass graticule ruler as feature points for further optimization. The world coordinates are calculated using the camera's internal and external parameters and the pixel coordinates of these points, and the ratio between the actual measured values and the theoretical values of the scale lines in the world coordinate system is calculated. If the ratio is close to 1, it indicates a better match between the camera's internal and external parameters and the model. This difference is used as the target, which is denoted as Ed.

This involves selecting two feature pixel points on the same scale line in the image to fit a line and calculate the distance to another fitted line in the world coordinate system.

Let pixel points A(xal1,yal1),B(xal2,yal2),C(xbl1,ybl1),D(xbl2,ybl2)

The transformation relationship between pixel points and world coordinates (xw,yw) is:

$$\begin{cases} x_w = x_w(P, x) \\ y_w = y_w(P, y) \end{cases} \tag{20}$$

Where P represents the camera's internal and external parameters, including:(tx,ty,tz,α,β,γ,f,k,sx,sy,cx,cy)。

The optimization function for the online measurement system described in this paper is:

$$\begin{aligned} E_d &= \frac{\left| y_{al1} - y_{bl1} + \frac{y_{al1} - y_{al2}}{x_{al1} - x_{al2}} y_{al1} - \frac{y_{bl1} - y_{bl2}}{x_{bl1} - x_{bl2}} y_{bl1} \right|}{d_{real}} \\ &= \frac{\left| \begin{array}{l} y_{w1}(P, y_{al1}) - y_{w3}(P, y_{bl1}) + \frac{y_{w1}(P, y_{al1}) - y_{w2}(P, y_{al2})}{x_{w1}(P, x_{al1}) - x_{w2}(P, x_{al2})} y_{w1}(P, y_{al1}) \\ - \frac{y_{w3}(P, y_{bl1}) - y_{w4}(P, y_{bl2})}{x_{w3}(P, x_{bl1}) - x_{w4}(P, x_{bl2})} y_{w3}(P, y_{bl1}) \end{array} \right|}{d_{real}} \end{aligned} \tag{21}$$

Where dreal is the theoretical scale value.

dreal takes the values 1000μm, 2000μm, 5000μm respectively. Under different values, Ed1, Ed2, and Ed5 are obtained, respectively.

The essence of optimizing P is to minimize Ed, i.e.:

$$\frac{dE_d}{dP} = 0 \tag{22}$$

This equation represents a complex nonlinear problem that cannot be solved analytically. The general solution process involves iteratively optimizing P until Ed is sufficiently small to yield an optimized result.

B. Response Surface Methodology

Response Surface Methodology (RSM), rooted in probability theory and statistics, addresses the intricate interplay between input and output variables within sophisticated systems. At its core, RSM assumes that when the precise relationship among one or multiple input variables and one or multiple output variables remains enigmatic, a precise yet approximate mathematical expression is constructed to articulate the linkage between input variables and the resulting outputs. This approach employs regression analysis to determine the unknown coefficients within the analytical expression, subsequently utilizing techniques such as variance and residual analysis to assess the regression model's validity. Once the model attains a satisfactory level of credibility, it can be leveraged to elucidate the functional linkage between input variables and output responses, facilitating optimization and prediction.

Basic Principle of Response Surface Methodology

The response surface method can be represented using the method of least squares estimation, and its approximate function can be constructed as follows:

$$\hat{y} = \beta_0 + \sum_{j=1}^{n} \beta_j x_j + \sum_{j=n+1}^{2n} \beta_j x_{j-n}^2 + \sum_{i=1}^{n-1} \sum_{j=j+1}^{n} \beta_{ij} x_i x_j \tag{23}$$

Where:

n is the number of design variables;

β_0 is the unknown coefficient for the constant term;

β_j is the unknown coefficient for the quadratic square term;

β_{ij} is the unknown coefficient for the quadratic cross term.

Using the method of substitution variables, let:

$$\begin{cases} x_0 = 1 \\ x_1 = x_1, x_2 = x_2, \ldots, x_n = x_n \\ x_{n+1} = x_1^2, x_{n+2} = x_2^2, \ldots, x_{2n} = x_n^2 \\ x_{2n+1} = x_1 x_2, x_{2n+2} = x_1 x_3, \ldots, x_{k-1} = x_{n-1} x_n \end{cases}$$

$$\begin{cases} \alpha_0 = \beta_0 \\ \alpha_1 = \beta_1, \alpha_2 = \beta_2, \ldots \alpha_n = \beta_n \\ \alpha_{n+1} = \beta_{n+1}, \alpha_{n+2} = \beta_{n+1}, \ldots \alpha_{2n} = \beta_{n+1} \\ x_{2n+1} = \beta_{12}, x_{2n+2} = \beta_{13}, \ldots \alpha_{k-1} = \beta_{(n-1)n} \end{cases}$$

Substituting into Equation (23), we get:

$$\hat{y} = \alpha_0 + \sum_{i=1}^{k-1} \alpha_i x_i \tag{24}$$

Where, α0,αi are undetermined coefficients.

As shown in Table 4, the number of αi, k, needs to be determined according to the type of constructed function in Equation (23).

Table 4: Number of αi

Approximate Function Form	k
Linear type	n-1
Separable quadratic type (without cross terms)	$2n$+1
Complete quadratic type	(n+1)(n+2)/2

To solve for αi, the number of independent experiments, h, must satisfy h ≥ k. Then, through h independent experiments, experimental data can be obtained, from which the unknown coefficients can be calculated by mathematical operations.

The calculation process is as follows:

$$x_1^{(l)} \ldots x_{k-1}^{(l)} y^{(l)}, l = 1,2,\ldots, h \tag{25}$$

Substituting (25) into (24) we get:

$$\hat{y}^{(l)} = \sum_{i=0}^{k-1} \alpha_i x_i^{(l)}, l = 1,2,\ldots h \tag{26}$$

The error between the function value of the response surface and the value obtained from the experiment is defined as:

$$\varepsilon = \left(\varepsilon_1, \varepsilon_2, \ldots, \varepsilon_h\right)^T$$

Then we have:

$$\varepsilon_h = \sum_{i=0}^{k=1} \alpha_i x_i^{(h)} - y^{(h)}, l = 1,2,\ldots h \tag{27}$$

To obtain the optimal response surface model using the least squares method, it is only necessary to minimize the sum of the squares of the errors:

$$S(\alpha) = \sum_{j=1}^{h} \varepsilon_j^2 = \sum_{j=1}^{h} \left[\sum_{i=0}^{k-1} \alpha_i x_i^{(j)} - y^{(j)} \right]^2 \rightarrow \min \tag{28}$$

Let:

$$\frac{\partial S}{\partial \beta_l} = 2\sum_{j=1}^{h}\left[x_i^{(j)}\left[\sum_{i=0}^{k-1}\alpha_i x_i^{(j)}\right]\right] = 0 \tag{29}$$

Equation (29) is a linear equation, which can be expressed as:

$$\sum_{j=1}^{h}\left[\sum_{i=0}^{s-1} x_{s-1}^{(j)}\alpha_i x_i^{(j)} - x_{s-1}^{(j)} y^{(j)}\right] = \sum_{i=0}^{s-1}\sum_{j=1}^{h} x_{s-1}^{(j)}\alpha_i - \sum_{j=1}^{h} x_{s-1}^{(j)} y^{(j)} = 0, s = 1,2,\ldots k \tag{30}$$

Matrix representation is:

$$(X\alpha - y)^T X = 0 \tag{31}$$

Where:

X is the matrix of independent variables;

Y is the vector of response surface values;

a is the vector of undetermined coefficients.

X, Y, and α have the following forms:

$$X = \begin{bmatrix} 1 & x_1^{(1)} & \cdots & x_{k-1}^{(1)} \\ 1 & x_1^{(2)} & \cdots & x_{k-1}^{(2)} \\ \vdots & \vdots & \cdots & \vdots \\ 1 & x_1^{(h)} & \cdots & x_{k-1}^{(h)} \end{bmatrix}, y = \begin{bmatrix} y^{(1)} \\ y^{(2)} \\ \vdots \\ y^{(h)} \end{bmatrix}, \alpha = \begin{bmatrix} \alpha_0 \\ \alpha_1 \\ \vdots \\ \alpha_{k-1} \end{bmatrix} \tag{32}$$

Thus, the expression for the response surface function can be obtained.

C. Response Surface Methodology Experimental Design

In this paper, there are a total of 12 parameters in the camera parameters, including internal and external parameters P (tx,ty,tz,α,β,γ,f,k,sx,sy,cx,cy). If the response surface method is used for the optimization process of all parameters, many groups of experiments would be required for analysis, leading to a large computational load and inconvenience for practical experiments. After calibrating the online measurement system for the melting pool morphology using Zhang's Calibration Method, a set of camera parameter values P0 has been obtained. Based on P0, this paper first analyzes the impact of fluctuations in individual parameter values on the Ed value. Table 5 shows the internal and external parameter values after camera calibration.

Table 5: Values of Various Parameters in P0

Parameter	Unit	Parameter Value	Parameter	Unit	Parameter Value
t_x	m	-0.023552	f	m	0.0381788
t_y	m	0.0104382	k	$1/m^2$	171.041
t_z	m	0.272155	s_x	m	6.3166e-06
α	°	336.696	s_y	m	7.00e-06
β	°	359.174	c_x	px	1144.59
γ	°	169.022	c_y	px	845.906

1) Single Parameter Experimental Analysis

Table 6: Range of Values for Various Parameters in P0

Parameter	Unit	Range (Lower Limit)	Range (Upper Limit)	Impact Degree
t_x	m	-0.023552	-0.023552	-
t_y	m	0.01	0.02	Significant
t_z	m	0.272155	0.272155	-
α	°	349.0	350.0	Significant
β	°	359.174	359.174	-
γ	°	169.022	169.022	-
f	m	0.0381788	0.0381788	-
k	$1/m^2$	171.041	171.041	-
s_x	m	6.0e-06	6.1e-06	Significant
s_y	m	7.00e-06	7.00e-06	-
c_x	px	1144.59	1144.59	-
c_y	px	845.906	845.906	-

In the single parameter analysis, this paper analyzes the impact of different parameters on calibration accuracy by varying the values of the 12 parameters (tx,ty,tz,α,β,γ,f,k,sx,sy,cx,cy) around the values shown in Table 5. The experimental calculation analysis shows that:

The parameters (ty,α,sx) among others significantly influence the calculation result of Ed;

With other parameter values fixed, the values of each parameter in Table 6 can bring the Ed value close to 1.

2) Establishment of Response Surface Experimental Mode

After completing the single parameter experimental analysis, the response surface experimental model is established. The experimental design involves effectively designing the experimental groups to ensure a high-precision experimental model while reducing the number of experimental groups and simplifying the design scheme. The experimental design methods for constructing the response surface include classical sampling methods and full-space distribution sampling methods. The classical sampling methods often used include orthogonal design, full/partial factor design, optimal design, uniform design, central composite design, Box-Behnken design, etc.

Based on the characteristics and accuracy requirements of this project, the response surface experimental design adopts the Box-Behnken design method. Based on the single parameter experimental analysis, (ty,α,sx) are used as the factors to be considered (X1,X2,X3), with Ed as the response value (Y1,Y2,Y3). The Box-Behnken experimental factors and levels are shown in Table 7, and the experimental results and analysis are shown in Table 8. This process is completed in Design Expert software.

Table 7: Box-Behnken Experimental Factors and Levels for Parameter Optimization

Factor	Factor	-1	0	1
t_y/m	X_1	0.01	0.015	0.02
α/°	X_2	349.0	349.5	350.0
s_x/μm	X_3	6.0	6.05	6.1

Table 8: Box-Behnken Experimental Results Analysis for Parameter Optimization

No.	t_y/m	α/°	s_x/μm	E_{d1}/μm	E_{d2}/μm	E_{d5}/μm
	X_1	X_2	X_3	Y_1	Y_2	Y_3
1	0.01	349	6.05	13.579	15.5347	26.2184
2	0.02	349	6.05	6.59144	1.47922	61.8178
3	0.01	350	6.05	13.9215	21.9591	9.68304
4	0.02	350	6.05	7.58156	9.24252	41.8915
5	0.01	349.5	6	21.8356	18.8304	17.7421
6	0.02	349.5	6	15.2271	5.44652	51.6393
7	0.01	349.5	6.1	5.66609	18.8251	17.75
8	0.02	349.5	6.1	1.05054	5.44129	51.647
9	0.015	349	6	18.2006	8.5098	44.0138
10	0.015	350	6	18.8613	15.6032	25.783
11	0.015	349	6.1	1.97179	8.50432	44.0216
12	0.015	350	6.1	2.64263	15.5979	25.7911
13	0.015	349.5	6.05	10.7511	15.6003	25.7872
14	0.015	349.5	6.05	19.4408	27.3926	30.7208
15	0.015	349.5	6.05	19.2086	19.9737	26.9447
16	0.015	349.5	6.05	16.2499	15.6003	23.1012
17	0.015	349.5	6.05	17.0868	21.7574	19.3747

Analyzing the experimental results shown in Table 10 using the response surface method model calculation and analysis can reveal the relationship between (ty,α,sx) and Ed1, Ed2, Ed5.

D. Response Surface Methodology Optimization Results

After fitting with the response surface methodology, the function model fitting conclusion meets expectations. The regression equation obtained is:

$$\begin{cases} Y_1 = 16.55 - 3.07X_1 + 0.3330X_2 - 7.85X_3 + 0.1619X_1X_2 + 0.4982X_1X_3 \\ + 0.0025X_2X_3 - 2.80{X_1}^2 - 3.33{X_2}^2 - 2.80{X_3}^2 \\ Y_2 = 20.06 - 6.69X_1 + 3.55X_2 - 0.0027X_3 + 0.3347X_1X_2 - 3.96{X_1}^2 \\ - 4.05{X_2}^2 - 3.96{X_3}^2 \\ Y_3 = 20.19 - 16.95X_1 - 9.12X_2 + 0.0039X_3 - 0.8477X_1X_2 - 0.0001X_1X_3 \\ - 0.0001X_2X_3 + 4.75{X_1}^2 + 1.57{X_2}^2 + 4.75{X_3}^2 \end{cases} \quad (33)$$

Variance analysis of the above equation yields the results shown in Table 9.

Table 9: Variance Analysis of Response Surface Methodology Experimental Results

Source of Variance	Sum of Squares	Degrees of Freedom	Mean Square	F-value	P-value	Significance
Y_1 Model	696.04	9	77.34	10.71	0.0025	Significant
Y_2 Model	684.38	9	76.04	5.52	0.0174	Significant
Y_3 Model	3294.70	9	366.08	35.49	<0.0001	Significant

From Table 8, the established models (Y1,Y2,Y3) are significant and highly reliable. Further stepwise regression of Equation (33) obtains the optimal parameter values for ((ty,α,sx)), and the optimized internal and external camera parameters are shown in Table 10:

Table 10: Optimized Internal and External Camera Parameters

Parameter	t_x	t_y	t_z	α	β	γ
Unit	m	m	m	°	°	°
Value	-0.023552	0.0103	0.272155	349.696	359.174	169.022
Parameter	f	k	s_x	s_y	c_x	c_y
Unit	m	$1/m^2$	m	m	px	px
Value	0.0381788	171.041	6.1e-06	7.00e-06	1144.59	845.906

IV. Experimental Verification and Result Analysis

Using the camera's internal and external parameters optimized by the response surface methodology, the measurement results obtained by extracting adjacent scales, two adjacent scales, and five adjacent scales from different images and poses captured by the camera are shown in Figure 7.

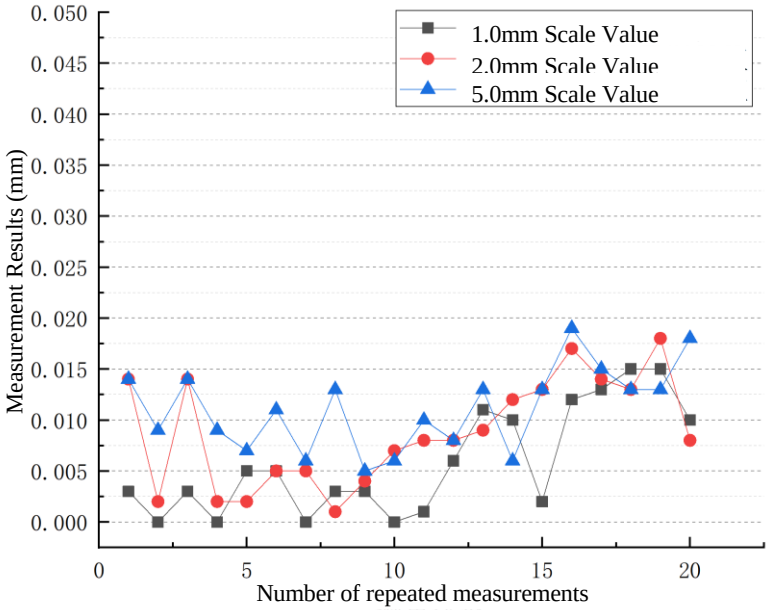

Figure 7: Measurement Results from Extracting Adjacent Scales

The thorough examination of errors in glass graticule ruler measurements across various positions reveals that the application of response surface methodology in optimizing camera parameters has yielded promising outcomes. Specifically, the measurement error is limited to 0.02mm, which adheres to the stringent precision standards for online monitoring of melting pool morphology during the additive manufacturing process of SLM equipment.

V. CONCLUSIONS

This paper addresses the accuracy needs of online measurement by calibrating the internal and external parameters of the camera in the online measurement system, performing error compensation and precision test analysis of the system. Based on Zhang's Calibration Method, the internal and external parameters of the camera for the online measurement system were calibrated. Using the response surface methodology, the internal and external parameters of the online measurement system camera were optimized. With a glass graticule ruler, technical indicator tests and analyses were conducted before and after error compensation of the online measurement system. Test results show that the online measurement system can meet the accuracy requirements for melting pool morphology in the SLM equipment additive manufacturing process.

Further research will focus on integrating the online measurement system for laser melting pool morphology into the upper computer control system of SLM equipment to achieve closed-loop feedback control, thereby improving the forming accuracy of workpieces. The software used in SLM is RP (Rapid Prototyping), whose main function is to import 3D CAD models, slice and layer the models according to process requirements, process the 2D slices with added process parameters, and generate numerical control codes for input into the SLM equipment former. The final product is formed by layer-by-layer accumulation in additive manufacturing. The RP software technology is relatively mature abroad, including SolidView, Magics, Rapid Prototyping Module, etc. Therefore, how to integrate the online measurement system with RP software to optimize SLM processing equipment is the next challenge to be addressed.

REFERENCES

[1] Wu Shibiao, Dou Wenhao. Research progress in detection technology for laser selective melting metal additive manufacturing. Precision Forming Engineering, 2019(7): 11-14.

[2] JOACHIM B, KARL H D, WILHELM S. Overview of Additive Manufacturing Activities at MTU Aero Engines//AIP Conference Proceedings. AIP Publishing, 2015:156-163.

[3] Li Ang, Liu Xuefeng. Key factors and development direction of metal additive manufacturing technology. Journal of Engineering Science, 2019(02), 41-42.

[4] Sun Changjin, Zhao Yuhui. Research on the development status and trends of non-destructive testing technology for new concept structures in additive manufacturing. Vacuum, 2019(07), 56-4.

[5] CLAIRE B R, ALI G D. Selective laser melting finite element modeling: Validation with high-speed imaging and lack of fusion defects prediction. Materials and Design, 156 (2018):143–153.

[6] Guo Jiaqi, Huang Anguo, Huang Kang, et al. Research status of online monitoring technology in electron beam wire feed additive manufacturing process Aeronautical Manufacturing Technology, 2018, 61(17):57-62.

[7] TIAN Y, TOMUS D, HUANG A, et al. Experimental and statistical analysis on process parameters and surface roughness relationship for selective laser melting of Hastelloy X. Rapid Prototyping Journal, 2019, 25(7):1309-1318.

[8] ROBICHAUD J, VINCENT T, SCHULTHEIS B, et al. Integrated computational materials engineering to predict melt-pool dimensions and 3D grain structures for selective laser melting of inconel625. Integrating Materials and Manufacturing Innovation, 2019, 8(3):305-317.

[9] KONG F, MA J, CARLSON, et al. Real-time monitoring of laser welding of galvanized high strength steel in lap joint configuration. Optics & Laser Technology, 2012, 44(7):2186-2196.

[10] TSAI R Y.A versatile camera calibration technique for high-accuracy 3D machine vision metrology using off-the-shelf TV camera and lens. IEEE journal of robotics and automation,1987,3(4).

[11] MA P M, HE X M, WANG A J. Design of Online Measurement System for Molten Pool Morphology in Selective Laser Melting. FCPAE2021 & 3rd International Conference on Artificial Intelligence and Advanced Manufacture,Manchester, UK, October, 2021.

[12] ZHANG Z Y. A flexible New Technique of Camera. IEEE Transactions on Pattern Analysis and Machine Intelligence, 2000,22(11):133~1334.

[13] WALID D, QUENTIN B, ADRIAN M. Plenoptic camera calibration based on microlens distortion modelling. ISPRS Journal of Photogrammetry and Remote Sensing, 2019, 158.